

---

This manuscript is a preprint that has been submitted to *Science Advances* and is currently under review. It has not yet received peer-review reports or been accepted for publication. Subsequent versions of this manuscript may have different content. If accepted, the final version of this manuscript will be available via the ‘Peer-reviewed Publication DOI’ link on the right-hand side of this webpage. Please feel free to contact the authors. We welcome feedback.

---

1 **Aquifer dynamics in the seismically active Salt Lake Valley, Utah, USA**

2 *Short title: Aquifer dynamics in Salt Lake Valley*

3 Xie Hu and Roland Bürgmann

4 Berkeley Seismological Laboratory, University of California, Berkeley, California 94720-4760,  
5 USA

6 Department of Earth and Planetary Science, University of California, Berkeley, California 94720-  
7 4767, USA

8 Correspondence to: xiehu@berkeley.edu

9

10 **Abstract:**

11 Aquifers and fault zones may interact through groundwater flow and stress redistribution, yet  
12 their spatiotemporal relationship remains enigmatic. Here we quantify changes in water storage  
13 and associated stress along the Wasatch Fault Zone in Salt Lake Valley, recently shaken by a  
14 M5.7 earthquake on March 18<sup>th</sup>, 2020. Ground deformation mapped by Sentinel-1 SAR imagery  
15 (2014-2019) reveals an elongated area with ~50-mm seasonal uplift corresponding to 0.03-0.06-  
16 km<sup>3</sup> water storage cycles. Phase shifts in water level and deformation across active faults suggest  
17 control by the low-permeability structures. The seasonal stress changes from poroelastic volume  
18 strain are two orders of magnitude larger than those from hydrological surface loading on the  
19 adjoining faults, but both are small compared to tectonic loading at seismogenic depths. Historic  
20 seismic events, limited in number, do not exhibit annual periodicity and hydrological modulation  
21 of microseismicity or triggering of the recent M5.7 event is not evident.

22

23 **INTRODUCTION**

24 Natural water discharge (e.g., evaporation and drainage) and recharge (e.g., rainfall and  
25 snowmelt infiltration) maintain a sustainable hydrosphere and ecosystem. In particular, aquifers  
26 help regulate the water balance by storing and releasing the groundwater as needed. Such natural  
27 subsurface reservoirs are invaluable in arid regions where freshwater resources are limited. Human  
28 extraction of groundwater is sustainable, if net extraction is balanced by recharge and water levels  
29 can be maintained at stable levels.

30 Land subsidence is often observed over sedimentary basins due to water level decline and  
31 gradual consolidation of the confining units and fine-grained silts and clays that constitute the  
32 interbeds. Subsidence may be large (up to several meters), permanent and unrecoverable  
33 (inelastic), if the water head drops below previously achieved lowest levels and the stress exceeds  
34 preconsolidation conditions (1, 2). Cyclic seasonal subsidence and uplift by millimeters to  
35 centimeters are typically associated with water discharge and recharge producing poroelastic  
36 deformation (e.g., 3-6). Horizontal movements also exist and generally occur in the vicinity of  
37 operating wells, near fault zones traversing aquifers, and along the margins of aquifer basins (e.g.,  
38 5, 7, 8). Consideration of the horizontal movements can improve our ability to quantify the  
39 properties and geometry of subsurface aquifer systems (9).

40 Hydrological loading and unloading may regulate seismicity through elastic stresses in the  
41 seismogenic zone (e.g., 10-12). In addition, poroelastic stresses due to subsurface pore-fluid  
42 pressure diffusion driven by precipitation and/or groundwater variations may also contribute to  
43 modulating seismicity, at least at shallow depths and in especially permeable rocks (e.g., 13-15).  
44 Anthropogenic oil and gas production and fluid injection may also trigger earthquakes through

45 pore pressure redistribution (e.g., 16-18). How natural groundwater processes in smaller  
46 sedimentary basins can affect seismic hazards remains an open question.

47 Salt Lake Valley, Utah is a sedimentary basin that hosts the commercial, industrial and  
48 financial state capital Salt Lake City. Three-fourths of the state's population (~3 million) is  
49 concentrated within a 160-km radius of the city. The valley is bounded by the generally NS-  
50 trending Oquirrh Mountains to the west, the Wasatch Range to the east, and the EW-trending  
51 Traverse Mountains to the south. The 70-km-long Jordan River traverses the central axis of the  
52 valley, connecting two remnants of prehistoric Lake Bonneville (30,000-14,000 yr BP) – Great  
53 Salt Lake and Utah Lake. The basins are composed of three distinct hydrological units (Fig. 1):  
54 the water discharge area with an upward hydraulic gradient in the lower-elevation northern part of  
55 the confined basin and a narrow unconfined zone bounding the Jordan River; the primary recharge  
56 area at the foot of the mountains where the hydraulic head gradient is downward; and the secondary  
57 recharge area in between where the confined and unconfined layers are not clearly distinguished  
58 (19).

59 The alluvial basins also host the parallel and sub-parallel N20°W trending Wasatch fault  
60 zone (WFZ) along the front of the Wasatch Range and the inner-valley West Valley fault zone  
61 (WVFZ), which make Salt Lake County one of the most seismically hazardous metropolitan areas  
62 in the interior of the western U.S. (20, 21). The 390-km-long WFZ extends from Malad City,  
63 Idaho, to Fayette, Utah along the western flank of the Wasatch Range, and separates the stable  
64 Rocky Mountains and Colorado Plateau to the east and the extending crust of the Basin and Range  
65 Province to the west (Fig. 1). The regression of Lake Bonneville and the deglaciation of mountain  
66 ranges around the WFZ during the Late Pleistocene to Early Holocene epochs caused lithospheric

67 rebound and accelerated the slip rates to  $\sim 1$  mm/yr, about twice as high as the average geologic  
68 slip rate on a  $10^5$  years time scale (22, 23).

69 Three en-echelon fault segments of the WFZ surrounding Salt Lake City include the Warm  
70 Springs fault (WSF), the East Bench fault (EBF), and the Cottonwood fault (CF) (24). The Salt  
71 Lake City segment of the WFZ is believed to produce large earthquakes (M 7.0+) every 1,300 to  
72 1,500 years, and the last one occurred about 1,400 years ago (25). The Utah Geological Survey  
73 and U.S. Geological Survey (2016) forecast a 93% likelihood of one or more moderate earthquakes  
74 of magnitude 5 or greater striking the Salt Lake Valley (SLV) in the next 50 years. Thus, the recent  
75 M5.7 Magna, Utah earthquake on March 18<sup>th</sup>, 2020 (Fig. 1C) was not a complete surprise.  
76 Earthquake hazard stems not only from the shaking, but also the potential liquefaction in lowland  
77 areas, and tsunami and seiches in Great Salt Lake if extensive ground subsidence were to occur  
78 due to rupture along the East Great Salt Lake fault (EGSLF) (25).

79 GPS measurements of horizontal motions in a stable North America reference frame  
80 indicate  $\leq \sim 1.6$  mm/yr of extension across the WFZ (26, 27). A map of dilatational strain rates (Fig.  
81 1) shows an accumulation of extension at  $0.1 \mu\text{strain/yr}$ . However, limited by the sparse  
82 distribution and inconsistent surveying time among the stations, GPS measurements alone are  
83 insufficient for the basin-wide characterization of deformation. Interferometric synthetic aperture  
84 radar (InSAR) provides complementary geodetic observations to monitor the spatially continuous  
85 crustal deformation with weekly to monthly updates, though the measurements are limited to one-  
86 dimensional line-of-sight (LOS). Here, we compile ascending (AT122) and descending (DT100)  
87 Sentinel-1 imagery (2014-2019) (fig. S1), and (semi-)continuous GPS observations (28; fig. S2)  
88 to decipher the multi-annual and seasonal vertical and horizontal motions in the SLV.

89 Wells provide a direct window into the subsurface hydrology. We use well data from the  
90 U.S. Geological Survey (<https://waterdata.usgs.gov/usa/nwis/>). Earthquake catalogues help us  
91 assess the potential effects from spatiotemporally variable stressing patterns. To assess spatio-  
92 temporal variations in seismicity, we draw on the decadal earthquake catalog from 1981 to 2018  
93 provided by the University of Utah (see supplement for details). A joint analysis of geodetic  
94 displacement measurements, water levels (fig. S3; table S1) and earthquake information (fig. S4;  
95 table S2) allows us to quantify the seasonal variation in water storage, the commensurate stress  
96 changes on nearby faults, and to explore the potential coupling between the hydrological and  
97 tectonic processes in the SLV.

98

## 99 **RESULTS**

### 100 **Regional seasonal and multi-annual deformation in space and time from InSAR**

101 We extract targets whose seasonal movements are predominantly vertical by correlating  
102 the timing of the LOS motions from ascending and descending data (see supplement). Strong  
103 vertical seasonal movements are mainly contained in the asymmetrical elongated area of interest  
104 (referred to as AOI hereafter), shown by white dashed outlines in Figs. 2B-D and fig. S5. Annual  
105 uplift peaks in the time-series displacements are generally around March to April. Our  
106 measurements can be validated by GPS station SUR1, the only site located inside the AOI in its  
107 southern part (Fig. 2). Although this station has less than 2 years of data available (1997-1998),  
108 the seasonal peak-to-peak motions are well resolved with amplitudes in the EW, NS and UD  
109 components of about 5.2, 2.9, and 27.4 mm, respectively (fig. S2). For comparison, the values for  
110 stations ZLC1 and SLCU at the margins of the AOI are about 11.4, 3.5, and 12.8 mm, and 14.1,  
111 7.7, 12.8 mm, respectively (Fig. 4), and the EW and UD components have similar amplitudes that

112 are much larger than in the NS direction. We project the 3D GPS displacements of ZLC1 into the  
113 Sentinel-1 LOS directions for comparison of time-dependent motions during 2014 to 2019 (Figs.  
114 2E, F). The GPS and InSAR time series match well with residuals of 2.58 and 1.00 mm for the  
115 AT122 and DT100 tracks, respectively. The time of year of peak uplift ( $\sim 4$  mm) at GPS sites on  
116 the surrounding ranges (i.e., COON and RBUT) occurs in summer/fall, while that for GPS sites  
117 within the basin-fill deposits occurs in winter/spring with larger amplitude.

118 We retrieve the 2D displacement maps (EW and vertical; Fig. 3) for seasonal amplitudes  
119 and multi-annual velocities from ascending and descending Sentinel-1 InSAR, assuming that the  
120 NS displacements are negligible (see supplement). The AOI presents pronounced seasonal motions  
121 in both horizontal and vertical components with sharp margins (Figs. 3C, D). The AOI uplifts by  
122  $\sim 50$  mm from fall to spring, accompanied by EW extension with a net horizontal motion of  $\sim 30$   
123 mm across the uplift zone. The displacements reverse for the other half of the year from spring to  
124 fall, with subsidence and EW shortening of the same magnitude. This N20°W oriented zone of  
125 hydrological deformation has a larger ( $\sim 600$  m) sediment thickness than the surrounding areas  
126 (29). The seasonal deformation zone is bounded by the WVFZ and EBF in the north, while the  
127 southern end without such bounding structures appears more diffuse in its deformation pattern.  
128 Hydrogeologically, the AOI is part of the water discharge unit. The Jordan River cuts  
129 longitudinally through the central AOI and divides the horizontal displacement field into several  
130 smaller, isolated patches.

131 The long-term displacement map for 2014-2019 reveals that the eastern half of the valley  
132 is subsiding at  $\sim 1$ -2 mm/yr relative to the western SLV. The spatial distribution of longer-term  
133 ground subsidence coincides with the areas of largest water level decline of  $\sim 12$  m along the  
134 eastern margins of the basin during 1985-2015 (fig. S3A; 30). Well data from 2015-2019 indicates

135 spatially variable water drawdown at up to 0.5 m/yr. In a small industrial area in North Salt Lake  
136 subsidence rates reach ~16 mm/yr (Fig. 3A and fig. S5), similar to Envisat ASAR results spanning  
137 2004-2010 (6). The seasonal displacement field highlights a local area experiencing highly  
138 variable aquifer storage, whereas the multi-annual displacement field presents a regional long-  
139 wavelength signal correlated with prolonged water drawdown.

#### 140 **Temporal variations of water levels and 3D GPS observations over the basin**

141 While the temporal sampling of water-level measurements is sparse, we are able to  
142 determine the phase and amplitude of average annual variations for some of the wells in the SLV  
143 region. The timing of the seasonal water level fluctuations varies among wells at different locations  
144 with phase shifts of several months (Fig. 4B and fig. S6). Wells located on either side of the EBF  
145 represent remarkably contrasting patterns in time. Artesian wells 23301 and 30901 in the water  
146 discharge area to the west of the EBF have the lowest water level from June to August, likely due  
147 to summer pumping. In contrast, this time period features the highest water levels at wells 94001  
148 and 03901 on the east side of the fault and in the water recharge area at the foot of the ranges (Fig.  
149 4B). Other wells distributed across the basin have varying temporal patterns that depend on their  
150 location with respect to the principal recharge and discharge zones and faults (figs. S3 and S6).

151 To further investigate the controls of the orientation and timing of seasonal displacements,  
152 we focus on three GPS time series that overlap in time (Fig. 4). Stations ZLC1 and SLCU are ~1.5  
153 km apart and located east of the WVFZ in the northeast portion of the AOI and within the water  
154 discharge area (confined aquifer), while UTCR is located on the southwestern edge of the AOI in  
155 the secondary recharge area just west of the WVFZ (undistinguished confined-unconfined  
156 aquifer). Seasonal uplift of UTCR is accompanied by southwesterly motion, whereas the uplift of  
157 ZLC1 and SLCU is accompanied by northeasterly motion, as expected for the expansion of a finite



158 elastic porous medium (e.g., 9). Interestingly, the seasonal displacements observed in those two  
159 groups are shifted by ~4 months: ZLC1 and SLCU have the largest subsidence in fall, in contrast  
160 to UTCR with peak subsidence in spring-summer. As for the 3D displacements of UTCR, the  
161 smallest horizontal motion (most southwesterly position) occurs up to 4 months earlier than that  
162 of the vertical component, while no evident difference in phase between the vertical and horizontal  
163 motions exists for the other two sites. Overall, the time-series GPS observations illuminate phase  
164 differences in 3D seasonal motions depending on the location in the groundwater basin, but the  
165 small number of stations limits our ability to make out systematic patterns in this behavior.

#### 166 **Relationship between seasonal water levels and GPS-/InSAR-derived displacements**

167 We attribute seasonal deformation patterns captured by the GPS and InSAR time series to  
168 annual variations in water storage in the SLV groundwater system, which is also reflected in the  
169 changing well water levels. Well 75901, southwest of the AOI and within the secondary recharge  
170 area (Fig. 2), is the only one that has daily sampled water levels during our observation period.  
171 The seasonal LOS displacements are relatively modest at this site (fig. S7). The peak  
172 displacements measured by both tracks are a few weeks prior to that of the water level. This may  
173 be because this well taps water at a depth of 242 m, above which there may be additional deforming  
174 layers whose water level changes earlier than the deeper aquifers.

175 The collocated GPS-derived ground motions and well water levels are correlated. For  
176 example, UTCR and its closest well #75901 reach their minima around May to June (Fig. 4), and  
177 the UTCR phase for 2011-2014 is consistent with that for Sentinel-1 in 2014-2019 (fig. S7). The  
178 storage coefficient describes the amount of water drained from the aquifer per unit decline in water  
179 level, and it can be resolved by a linear correlation between the vertical displacements and water  
180 level changes (ref. 5 and references cited there). The regional storage coefficient at SLV is between

181 0.002 and 0.07, and  $\sim 0.024$  near downtown Salt Lake City (6). Referring to the seasonal vertical  
182 displacement of the AOI, we estimate that the principal aquifer experiences up to  $\sim 3$  m of seasonal  
183 water-level variations, corresponding to up to  $\sim 1$  m of equivalent-water-thickness and seasonal  
184 change in water storage of  $\sim 0.045$  km<sup>3</sup>, considering a porosity of 0.2-0.4. Such hydrological  
185 loading can produce up to 6 mm elastic subsidence in the spring (reversed for the unloading  
186 scenario; fig. S8) (31), which is negligible compared to the 50-mm vertical motion due to the  
187 expansion and contraction of the aquifer skeleton. Note that the direction of the vertical motions  
188 from these two physical processes, associated with seasonal water storage change (i.e., poroelastic  
189 volume strain) and elastic loading, are opposite of one another.

190

## 191 **DISCUSSION**

### 192 **Deformation from elastic loading vs. poroelastic aquifer strain**

193 The timing difference in cyclic ground motions between the mountain ranges and the  
194 adjacent unconsolidated alluvial basins are well understood as a consequence of their distinct  
195 controlling mechanisms (e.g., 32). Elastic loading and unloading by snow and water result in  
196 instantaneous ground subsidence and uplift as illustrated by the GPS stations located on the ranges  
197 (RBUT and COON in Fig. 2 and fig. S2). On the other hand, groundwater inflow and outflow in  
198 the basin environment cause poroelastic uplift and subsidence, respectively, generally with delays  
199 due to diffusion of water into and out of the aquifer and/or inelastic compaction processes. When  
200 hydraulic head declines, groundwater outflows from pore spaces in the fine-grained interbeds and  
201 confining units, and thus the compressible materials elastically compact and the land subsides. The  
202 opposite phenomenon occurs when hydraulic head increases, raising pore fluid pressure and  
203 decreasing the effective elastic stress on the granular skeleton supporting the vertical load (e.g, 5,

204 33). Therefore, land surface elevations above the aquifer reach maxima during snowmelt runoff  
205 from the mountains and reach minima when groundwater levels are depleted by surface and  
206 subsurface flow, pumping, and evaporation.

### 207 **Role of fault-aquifer interaction**

208 Multiple evidence suggests that faults may act as physical boundaries, defining and perhaps  
209 controlling groundwater redistribution. In the spatial domain, the margins of the AOI agree with  
210 the extent of the confined water discharge area and nearby active fault traces. The Jordan River  
211 cutting through the AOI longitudinally also affects the groundwater system and complicates the  
212 displacement field in the center of the AOI. In the temporal domain, different sides of the fault  
213 splays have distinct phase patterns in their seasonal motions and also in water level (Fig. 4 and fig.  
214 S6). The faults and fractures at depth may act as low-permeability barriers to horizontal flow, so  
215 the groundwater flow is regulated but not completely obstructed. This may be the reason for the  
216 observed phase shift by several months of the water levels on either side of the EBF (fig. S6), and  
217 phase differences in ground motions between the two sides of the WVFZ (Fig. 2).

### 218 **Estimating water storage and volume strain changes**

219 To estimate the water storage changes and quantify the stress contribution from the  
220 seasonal deformation of the aquifer system, we rely on an analytical solution of finite strain  
221 volumes in a half-space for cuboid sources (34). We mesh the AOI using an arrangement of 481  
222 grids with individual dimensions of 500- by 500-m, striking N20°W, sub-parallel to the basin  
223 and surrounding fault strands. Here we consider isotropic volume-strain sources reaching up to  
224 the surface, assuming that any shallow confining layer is thin. As a first-order approximation of  
225 the isopach map of unconsolidated and semi-consolidated sediments over this AOI (29), we  
226 assume a bulk aquifer thickness of up to 600 m and apply a Poisson's ratio of 0.25.

227           There is a strong trade-off between the volume strain and thickness of the model cuboids.  
228   We thus consider two end-member scenarios of constant volume strain and variable thickness,  
229   and variable strain and constant thickness of the cuboid elements to generate best-fit LOS  
230   displacement fields, which capture both the vertical and horizontal motions (figs. S9 and S10).  
231   We focus on the skeleton expansion during the wintertime phase of peak uplift. In the first  
232   model, assuming that the vertical motion linearly correlates with the water level and thus the  
233   aquifer bulk thickness, we use the InSAR-resolved vertical seasonal amplitudes to obtain aquifer  
234   thicknesses ranging from 0 to 600 m. A homogeneous isotropic strain of  $9.1 \times 10^{-5}$  yields 3D  
235   displacements that best fit the ascending and descending InSAR observations. In the second end-  
236   member model, we consider a constant aquifer thickness of 500 m for all the cuboids and  
237   compute the displacement fields generated by unit volume-strain from each cuboid. We invert  
238   for the distribution of volume strain that produces a displacement field that best fits the InSAR  
239   results, and the resulting strains range from  $\sim 2-12 \times 10^{-5}$ . This model has slightly smaller residuals  
240   than the variable thickness model (fig. S9). The distribution of the uplift and thus the bulk  
241   thickness in the first model and that of the strain in the second model are very similar, suggesting  
242   consistent vertical integration of the strain sources. The consequent seasonal bulk volume change  
243   for these two models is estimated to be  $3.3 \times 10^6$  and  $3.5 \times 10^6$  m<sup>3</sup>, respectively, similar to the  
244   product of the previously estimated representative storage coefficient ( $\sim 0.024$ ) and the  
245   volumetric variation of the water-bearing unit ( $1.5 \times 10^8$  m<sup>3</sup>).

#### 246   **Stress changes from volume strain and elastic surface loading**

247           Using the volume-strain sources from the variable-strain model inverted from the seasonal  
248   deformation data, we can forward model the seasonal changes in stress on nearby faults, assuming  
249   a shear modulus of 3 GPa for the young basement. Accompanying annual surface uplift of  $\sim 50$

250 mm and water storage increase of 0.03-0.06 km<sup>3</sup>, the estimated Coulomb stresses on the dipping  
251 fault planes (WSF, EBF and CF) change by about -450 to 50 kPa at shallow depth (<~600 m)  
252 during the wintertime (peaking in March); the stress changes reverse for the summertime (Fig. 5C  
253 and fig. S11). In the normal-faulting regime, larger earthquakes tend to nucleate near the brittle-  
254 ductile transition zone (>10 km) and propagate upwards (35). At these depths, the stress  
255 perturbations from the nontectonic aquifer strain are about -10 to 2 kPa during the wintertime.  
256 Overall, the seasonal stress changes in the spring are dominated by negative normal stress changes  
257 (clamping) underlying the aquifer and larger positive normal stress changes (unclamping) at the  
258 sides on dipping faults (fig. S11). The seasonal stress changes at seismogenic depths due to shallow  
259 aquifer processes generally lie below estimates of the annual background loading rate on the WFZ  
260 (~15 kPa/yr; 36). Note that a wide range of elastic moduli in the natural basin and range setting  
261 brings uncertainty to the absolute values of our stress-change estimates.

262 In addition to aquifer deformation, seasonal stress variations also result from other  
263 hydroclimatic periodic sources, including elastic water loads, atmospheric pressure, temperature,  
264 and Earth pole tides (e.g., 11). In California, the largest regional source of seasonal stressing comes  
265 from elastic water loads in the form of snow, lakes and groundwater and may periodically increase  
266 seismicity rates by nearly 10% (11). For a first-order estimate of stress changes at depth due to  
267 elastic loading, we model deformation and stress from the Salt Lake Valley aquifer storage changes  
268 by applying an equivalent line load rate of  $(2.58 \pm 0.29) \times 10^7 \text{ N} \cdot \text{m}^{-1}$  distributed across the width of  
269 the deforming aquifer (see supplement) (32, 37, 38). We find that the Coulomb stress changes  
270 during peak spring loading on a fault plane dipping 55° (26) are up to 3.2 kPa at the edge of the  
271 loading source and decrease dramatically to <<1 kPa at a depth of >10 km due to the narrow load  
272 dimension of 8 km (Fig. 6). These values are insignificant compared to background stress and

273 stressing-rate levels. Overall, the stress change from the elastic volume strain source at shallow  
274 depth is more than two orders of magnitude larger than that from the surface loading.

### 275 **Seismicity analysis to assess role of annual and multi-year stress perturbations**

276 The 1981-2018 earthquake catalog for the SLV contains a total of 635 seismic events, up  
277 to M4.16 (Fig. 5A). After declustering the catalogue, we are left with 512 events (see supplement;  
278 39). The major faults of the WFZ do not host a significant number of events. Instead, the northwest  
279 SLV contains two major clusters (Fig. 5). Cluster *a* is bounded by splays of the WVFZ. Cluster *b*  
280 is separated by the WVFZ and lies ~7 km west of *a* and at a greater depth (~8 versus ~5 km), in  
281 the hanging wall of the deep extension of the WSF and EBF. The time series displacements over  
282 cluster *a* indicate regular seasonal variations with a peak around May (Fig. 5B), whereas motions  
283 above cluster *b*, near the recent M5.7 earthquake, are fairly stochastic (fig. S12). The second  
284 invariant of the seasonal stress changes ( $\sqrt{|\Delta I_2|}$ ) from the aquifer strain  $\sqrt{|\Delta I_2|}$  at the hypocenters  
285 reaches up to ~20 kPa in cluster *a* while stress changes are low (<3 kPa) in the more distant cluster  
286 *b*. The March 18<sup>th</sup>, 2020 M5.7 earthquake  
287 (<https://earthquake.usgs.gov/earthquakes/eventpage/uu60363602/origin/detail>) is located within  
288 cluster *b* and the springtime Coulomb stress changes on 55° west-dipping normal faults near the  
289 hypocenter are 0.36 kPa and 0.1 kPa from the volume strain and surface loading, respectively.

290 Unlike the apparent seasonal variation in seismicity rates due to regional hydrological load  
291 cycles in the Nepal Himalayas (40), California (11, 32), and the New Madrid Seismic Zone (12),  
292 more than one annual peak of seismicity is present in the SLV (Fig. 5B). While the volume  
293 expansion and loading of the principal aquifer peak in spring (Figs. 2B, D), with decreased  
294 Coulomb stress concentrated at ~0-1 km to discourage failure and with increased Coulomb stress  
295 at depth of ~1-4 km to promote failure on the WSF and EBF (Fig. 5C), we are not able to resolve

296 corresponding seasonal changes in seismicity rates in clusters *a* and *b* that would support a direct  
297 triggering relationship.

298 On a multi-decadal timescale, while there are temporal variations in both precipitation  
299 (proxy for groundwater level) and the number of earthquakes, there does not appear to be a  
300 significant correlation (fig. S4). The limited number of events during four decades over the ~700-  
301 km<sup>2</sup> SLV basin may simply be insufficient to decipher the code of nature with confidence,  
302 compared to the significant seasonality seen in orders-of-magnitude larger seismicity catalogs in  
303 Nepal, California and New Madrid (11, 12, 40). In future work, we hope to explore the role of  
304 regional hydrological loading and unloading across the larger Wasatch Range front area, including  
305 contributions of regional seasonal snow loads and highly variable levels of the Great Salt Lake.

## 306 **Summary**

307 To sum up, we map out a multi-annual subsidence coinciding with prolonged water level  
308 decline in the eastern SLV along the front of the Wasatch Range. We also identify an elongated  
309 aquifer following a regular peak-to-peak seasonal uplift (50 mm) and extension (30 mm) during  
310 wintertime (reversed for summertime), revealing a seasonal variation in water storage by ~0.03-  
311 0.06 km<sup>3</sup>. The spatial association of the seasonally deforming area, hydrological discharge units  
312 and fault splays, as well as phase shifts in the displacement time series and water levels in areas  
313 separated by active faults, indicate that the faults modulate the groundwater flow and poroelastic  
314 strain field. The seasonal groundwater breathing of the aquifer exerts up to a few kPa Coulomb  
315 stress from the poroelastic volume strain and elastic loading at seismogenic depth of nearby fault  
316 zones, generally below the annual increase of tectonic stress. There is currently no evidence to  
317 suggest that earthquakes in the SLV, including the March 18<sup>th</sup>, 2020, M5.7 Magna earthquake, are  
318 directly related to the seasonal or multi-year aquifer deformation processes.

319 **References and Notes:**

- 320 1. D. L. Galloway, T. J. Burbey, Review: Regional land subsidence accompanying  
321 groundwater extraction. *Hydrogeology Journal* **19**(8), 1459–1486 (2011).
- 322 2. C. Ojha, M. Shirzaei, S. Werth, D. F. Argus, T. G. Farr, Sustained groundwater loss in  
323 California’s Central Valley exacerbated by intense drought periods. *Water Resources*  
324 *Research* **54** (2018).
- 325 3. F. Amelung, D. L. Galloway, J. W. Bell, H. A. Zebker, R. J. Laczniak, Sensing the ups  
326 and downs of Las Vegas: InSAR reveals structural control of land subsidence and  
327 aquifer-system deformation. *Geology* **27**(6), 483-486 (1999).
- 328 4. Z. Lu, W. R. Danskin, InSAR analysis of natural recharge to define structure of a ground-  
329 water basin, San Bernardino, California. *Geophys. Res. Lett.* **28**(13), 2661-2664 (2001).
- 330 5. E. Chaussard, R. Bürgmann, M. Shirzaei, E. J. Fielding, B. Baker, Predictability of  
331 hydraulic head changes and characterization of aquifer system and fault properties from  
332 InSAR-derived ground deformation. *J. Geophys. Res.* **119**, 6572-6590 (2014).
- 333 6. X. Hu, Z. Lu, T. Wang, Characterization of hydrogeological properties in Salt Lake  
334 Valley, Utah using InSAR. *J. Geophys. Res.* **123** (2018).
- 335 7. D. C. Helm, Horizontal aquifer movement in a Theis-Thiem confined system. *Water*  
336 *Resour. Res.* **30**(4), 953–964 (1994).
- 337 8. Y. Fu, D. F. Argus, J. T. Freymueller, M. B. Heflin, Horizontal motion in elastic response  
338 to seasonal loading of rain water in the Amazon Basin and monsoon water in Southeast  
339 Asia observed by GPS and inferred from GRACE. *Geophys. Res. Lett.* **40**, 6048–6053  
340 (2013).
- 341 9. T. J. Burbey, The influence of geologic structures on deformation due to ground water  
342 withdrawal. *Ground Water* **46**(2), 202–211 (2008).
- 343 10. P. González, K. Tiampo, M. Palano, F. Cannavó, José Fernández, The 2011 Lorca  
344 earthquake slip distribution controlled by groundwater crustal unloading. *Nature Geosci.*  
345 **5**, 821–825 (2012).
- 346 11. C. W. Johnson, Y. Fu, R. Bürgmann, Stress models of the annual hydrospheric,  
347 atmospheric, thermal, and tidal loading cycles on California faults: perturbation of



- 348 background stress and changes in seismicity. *J. Geophys. Res.* **122**, 10,605–10,625  
349 (2017).
- 350 12. J. Craig, K. Chanard, E. Calais, Hydrologically-driven crustal stresses and seismicity in  
351 the New Madrid Seismic Zone. *Nat. Commun.* **8**, 2143 (2017).
- 352 13. S. Hainzl, T. Kraft, J. Wassermann, H. Igel, E. Schmedes, Evidence for rainfall-triggered  
353 earthquake activity. *Geophys. Res. Lett.* **33**, L19303 (2006).
- 354 14. E. K. Montgomery-Brown, D. R. Shelly, P. A. Hsieh, Snowmelt-triggered earthquake  
355 swarms at the margin of Long Valley Caldera, California. *Geophys. Res. Lett.* **46**, 3698–  
356 3705 (2019).
- 357 15. N. Wetzler, E. Shalev, T. Göbel, F. Amelung, I. Kurzon, V. Lyakhovsky, E. E. Brodsky,  
358 Earthquake swarms triggered by groundwater extraction near the Dead Sea Fault.  
359 *Geophys. Res. Lett.* **46**, 8056–8063 (2019).
- 360 16. W. Ellsworth, Injection-Induced Earthquakes. *Science* **341** (2013).
- 361 17. M. Shirzaei, W. L. Ellsworth, K. F. Tiampo, P. J. González, M. Manga, Surface uplift  
362 and time-dependent seismic hazard due to fluid injection in eastern Texas. *Science* **353**,  
363 1416 (2016).
- 364 18. T. H. W. Goebel, E. E. Brodsky, The spatial footprint of injection wells in a global  
365 compilation of induced earthquake sequences. *Science* **361**(6405), 899-904 (2018).
- 366 19. S. A. Thiros, L. M. Bexfield, D. W. Anning, J. M. Huntington, “Section 2-Conceptual  
367 Understanding and groundwater quality of selected basin-fill aquifers in the southwestern  
368 United States” (U.S. Geol. Survey Prof. Paper 1781, 2010).
- 369 20. I. Wong, W. Silva, S. Olig, P. Thomas, D. Wright, F. Ashland, N. Gregor, J. Pechmann,  
370 M. Dober, G. Christenson, R. Gerth, “Earthquake scenario and probabilistic ground  
371 shaking maps for the Salt Lake City, Utah, metropolitan area” (Utah Geological Survey  
372 Miscellaneous Publication MP-02- 05, 2002).
- 373 21. A. Valentini, C. B. DuRoss, E. H. Field, R. D. Gold, R. W. Briggs, F. Visini, B. Pace,  
374 Relaxing segmentation on the Wasatch Fault Zone: impact on seismic hazard. *Bull.*  
375 *Seismol. Soc. Am.* **110**(1), 83–109 (2020).
- 376 22. R. Hetzel, A. Hampel, Slip rate variations on normal faults during glacial–interglacial  
377 changes in surface loads. *Nature* **435**, 81–84 (2005).

- 378 23. A. Hampel, R. Hetzel, G. Maniatis, Response of faults to climate-driven changes in ice  
379 and water volumes on Earth's surface. *Philosophical Transactions of the Royal Society*  
380 *A: Mathematical, Physical and Engineering Sciences* **368**, 1919, 2501–2517 (2010).
- 381 24. M. P. Moschetti, S. Hartzell, L. Ramírez-Guzmán, A. D. Frankel, S. J. Angster, W. J.  
382 Stephenson, 3D ground-motion simulations of Mw 7 earthquakes on the Salt Lake City  
383 segment of the Wasatch Fault Zone: variability of long-period ( $T \geq 1$  s) ground motions  
384 and sensitivity to kinematic rupture parameters. *Bull. Seismol. Soc. Am.* **107**(4), 1704–  
385 1723 (2017).
- 386 25. Earthquake Engineering Research Institute, Utah Chapter, “Scenario for a Magnitude 7.0  
387 Earthquake on the Wasatch Fault–Salt Lake City Segment” (Prepared for the Utah  
388 Seismic Safety Commission, 2015). [https://dem.utah.gov/wp-](https://dem.utah.gov/wp-content/uploads/sites/18/2015/03/RS1058_EERI_SLC_EQ_Scenario.pdf)  
389 [content/uploads/sites/18/2015/03/RS1058\\_EERI\\_SLC\\_EQ\\_Scenario.pdf](https://dem.utah.gov/wp-content/uploads/sites/18/2015/03/RS1058_EERI_SLC_EQ_Scenario.pdf)
- 390 26. W.-L. Chang, R. B. Smith, C. M. Meertens, R. A. Harris, Contemporary deformation of  
391 the Wasatch Fault, Utah, from GPS measurements with implications for interseismic fault  
392 behavior and earthquake hazard: observations and kinematic analysis. *J. Geophys. Res.*  
393 **111** (2006).
- 394 27. T. A. Herring, T. I. Melbourne, M. H. Murray, M. A. Floyd, W. M. Szeliga, R. W. King,  
395 D. A. Phillips, C. M. Puskas, M. Santillan, L. Wang, Plate Boundary Observatory and  
396 related networks: GPS data analysis methods and geodetic products. *Rev. Geophys.* **54**  
397 (2016).
- 398 28. G. Blewitt, C. Kreemer, W. C. Hammond, J. M. Goldfarb, Terrestrial reference frame  
399 NA12 for crustal deformation studies in North America. *J. Geodynamics* **72**, 11–24  
400 (2013).
- 401 29. R. E. Mattick, “Thickness of unconsolidated to semiconsolidated sediments in Jordan  
402 Valley, Utah” (U.S. Geol. Survey Prof. Paper 700-C, C119-C124, 1970).
- 403 30. C. B. Burden, et al., “Ground-water conditions in Utah” (Utah Department of Natural  
404 Resources Division of Water Resources Cooperative Investigations Report Number 56,  
405 2015).
- 406 31. J. M. Becker, M. Bevis, Love's problem. *Geophys. J. Int.* **156**, 171–178 (2004).

- 407 32. C. B. Amos, P. Audet, W. C. Hammond, R. Bürgmann, I. A. Johanson, G. Blewitt, Uplift  
408 and seismicity driven by groundwater depletion in central California. *Nature* **509**, 483–  
409 486 (2014).
- 410 33. J. R. Rice, M. P. Cleary, Some basic stress diffusion solutions for fluid saturated elastic  
411 porous media with compressible constituents. *Rev. Geophys.* **14**, 227–241 (1976).
- 412 34. S. Barbot, J. D. P. Moore, V. Lambert, Displacement and Stress Associated with  
413 Distributed Anelastic Deformation in a Half-Space. *Bull. Seismol. Soc. Am.* **107**(2), 821–  
414 855 (2017).
- 415 35. D. Roten, K. B. Olsen, J. C. Pechmann, V. M. Cruz-Atienza, H. Magistrale, 3D  
416 simulations of M7 earthquakes on the Wasatch Fault, Utah, Part I: long-period (0–1 Hz)  
417 ground motion. *Bull. Seismol. Soc. Am.* **101**(5), 2045–2063 (2011).
- 418 36. M. Bagge, A. Hampel, R. D. Gold, Modeling the Holocene slip history of the Wasatch  
419 fault (Utah): coseismic and postseismic Coulomb stress changes and implications for  
420 paleoseismicity and seismic hazard. *GSA Bulletin* **131**, 43–57 (2019).
- 421 37. J. Jaeger, N. Cook, R. Zimmerman, *Fundamentals of Rock Mechanics* (4th ed, Blackwell,  
422 2007).
- 423 38. Kundu, B., N. K. Vissa, V. K. Gahalaut, Influence of anthropogenic groundwater  
424 unloading in Indo-Gangetic plains on the 25 April 2015 Mw 7.8 Gorkha, Nepal  
425 earthquake. *Geophys. Res. Lett.* **42**, 10,607–10,613 (2015).
- 426 39. S. Wiemer, A software package to analyze seismicity: ZMAP. *Seism. Res. Lett.* **72**(3),  
427 373–382 (2001).
- 428 40. P. Bettinelli, et al., Seasonal variations of seismicity and geodetic strain in the Himalaya  
429 induced by surface hydrology. *Earth Planet. Sci. Lett.* **266**, 332–344 (2008).

430 **Acknowledgments:**

431 We thank Rishav Mallick, Sylvain Barbot, Yuning Fu, Xue Liang, Kathryn Materna, Chi-yuen  
432 Wang, and Taka’aki Taira for helpful discussions on this work. We thank Nevada Geodetic  
433 Laboratory for providing GPS time-series products over the Salt Lake Valley; UVAVCO for  
434 providing GPS velocities for the eastern Basin-Range province; Utah Automated Geographic  
435 Reference Center (AGRC) for providing the locations of recharge and discharge areas of the  
436 principal aquifers along the Wasatch Front and adjacent areas, as well as the location of Quaternary  
437 faults; U.S. Geological Survey (USGS) for providing water level data; University of Utah  
438 Seismograph Stations for providing earthquake catalogue. This research was sponsored by the  
439 NASA Earth Surface and Interior grant NNX17AE01G.

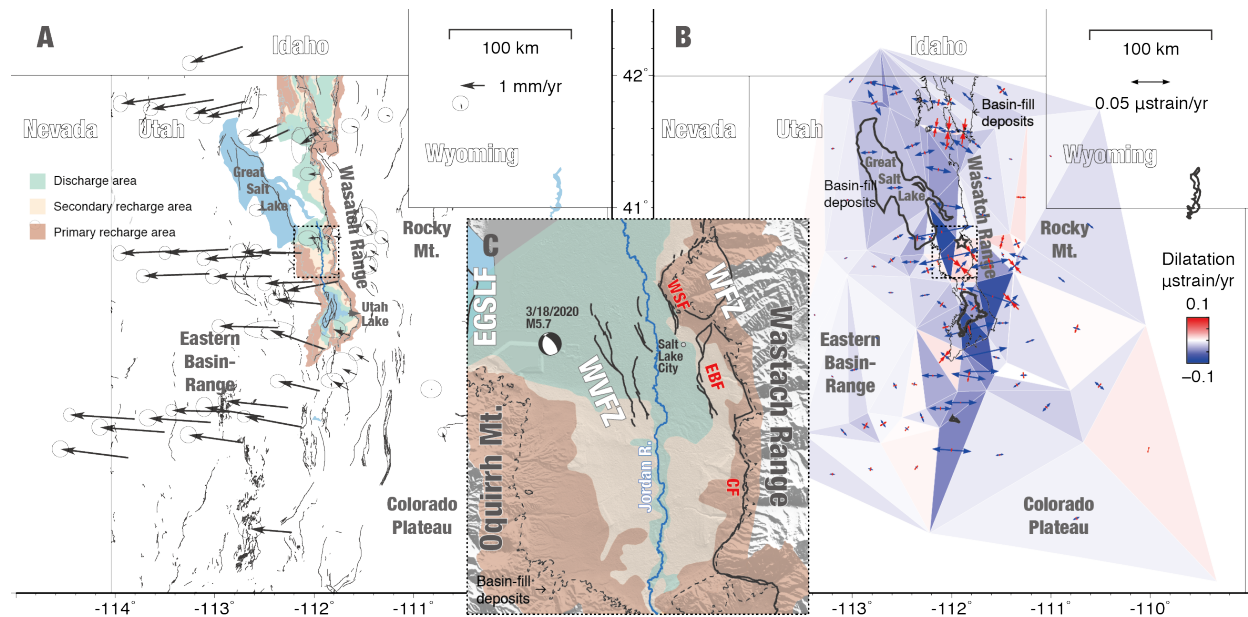
440

441 **Supplementary Materials:**

442 Materials and Methods

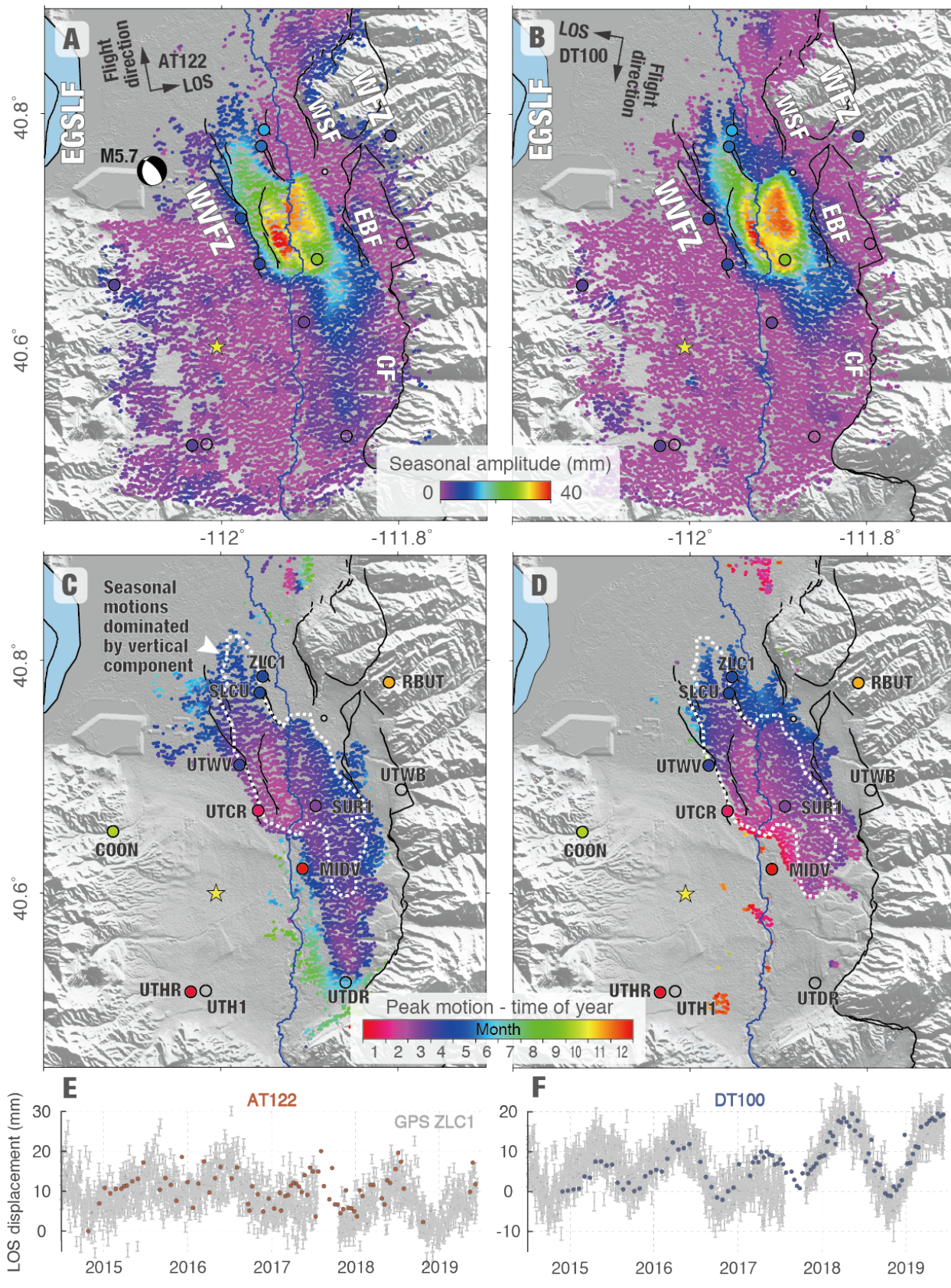
443 Figures S1-S12

444 Tables S1-S2

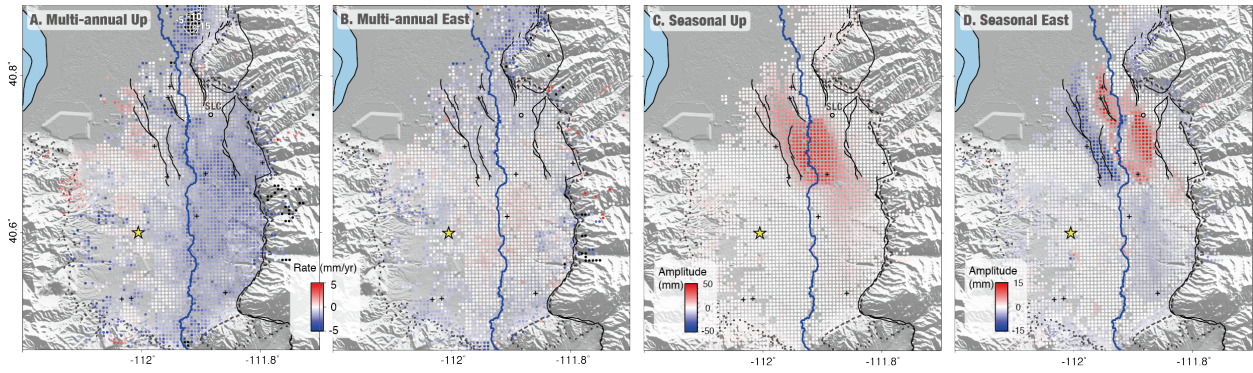


445

446 Figure 1. Map of a part of the eastern Basin and Range Province. (A) The distribution of water  
 447 discharge, primary recharge and secondary recharge areas of the principal aquifers are  
 448 differentiated by colors. Arrows show the horizontal velocity vectors of continuously operating  
 449 GPS stations in a stable North America reference frame (27). The error ellipses represent 95%  
 450 confidence intervals. Black lines are the Quaternary faults. (B) The horizontal strain-rate field  
 451 determined from the GPS velocities. Arrows represent the direction of the principal strains.  
 452 Dilatational strain (blue) governs most parts of the eastern Basin-Range. Our study area, Salt Lake  
 453 Valley (SLV), is highlighted by a dashed box in the center of panels A and B. (C) A close-up view  
 454 of SLV. Dashed black lines delineate the boundary of basin-fill deposits. Blue line shows the  
 455 Jordan River. Solid black lines show the faults. Faults in the SLV include the West Valley fault  
 456 (WVF), the East Great Salt Lake fault (EGSLF), and the Wasatch fault zone (WFZ), including  
 457 three major Salt Lake City segments – the Warm Springs fault (WSF), East Bench fault (EBF),  
 458 and Cottonwood fault (CF). The epicenter of the M5.7 Magna earthquake west of the WVFZ is  
 459 shown by its normal-faulting focal mechanism.



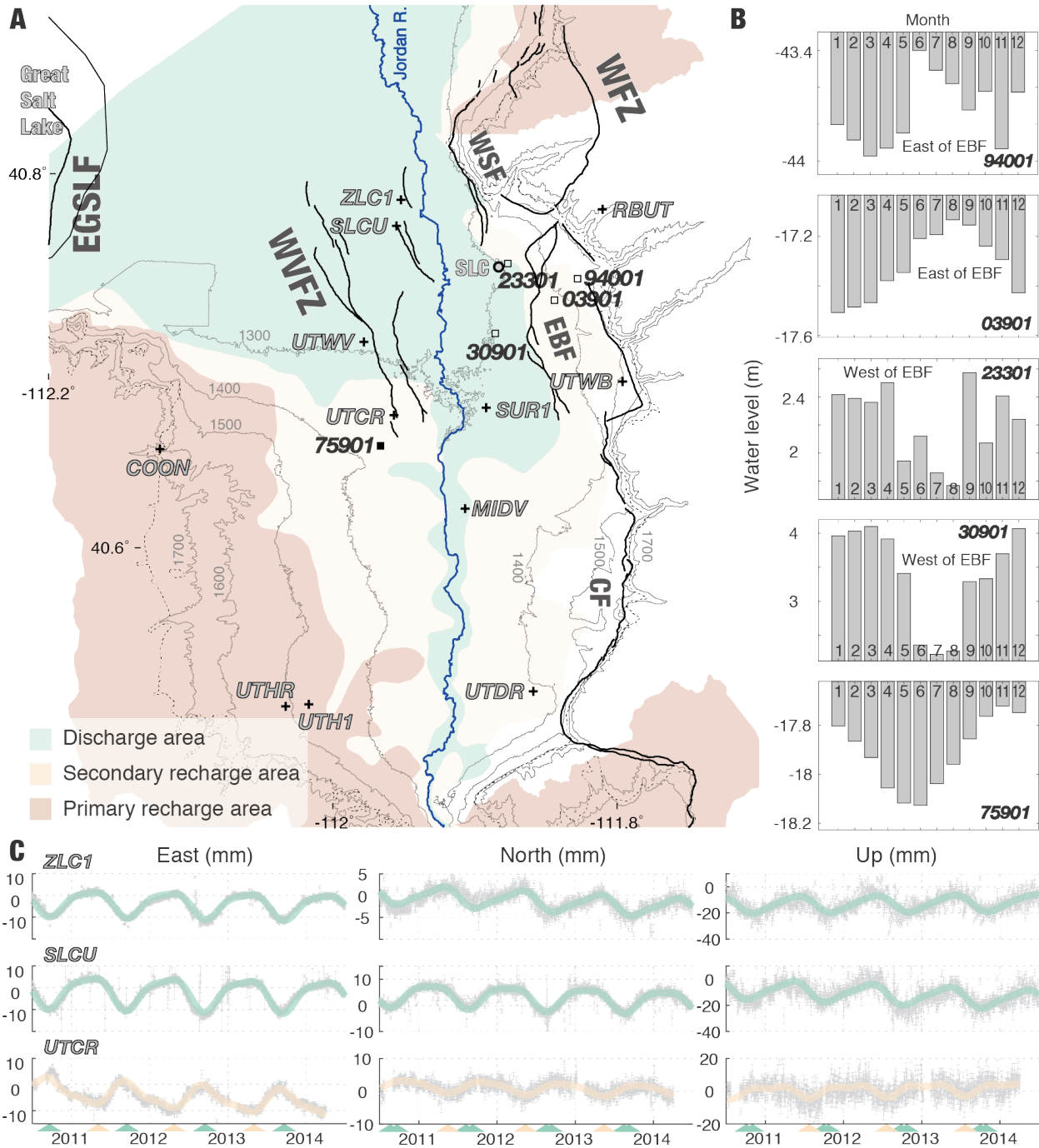
461 Figure 2. Seasonal deformation of Salt Lake Valley from 2014-2019 Sentinel-1 InSAR time series.  
462 (A) and (B) show the characteristic seasonal peak-to-peak amplitude measured along the line-of-  
463 sight (LOS) of tracks AT122 and DT100, respectively. (C) and (D) show the average time of year  
464 of the seasonal LOS minimum (consistent with peak uplift) for targets whose seasonal amplitude  
465 is larger than 1 mm. Colored circles (with station labels in C and D) represent the amplitude and  
466 phase information obtained from the time series of the vertical GPS component; unfilled circles  
467 are stations whose seasonal uplift was not resolved due to short time spans. White dotted lines  
468 highlight the area with seasonal motions dominated by the vertical component. (E) and (F)  
469 compare Sentinel-1 LOS and GPS time series during 2014-2019. The 3D GPS displacement time  
470 series at station ZLC1 in gray symbols have been projected into radar LOS directions for  
471 comparison with ascending track AT122 (red circles) and descending DT100 (blue circles) LOS  
472 time series at the same location.



473

474 Figure 3. Two-dimensional (up and east) velocities and seasonal displacements. (A) Uplift rate  
 475 and (B) east velocity during 2014-2019. (C) Seasonal uplift and (D) east displacement amplitude  
 476 during wintertime. The yellow star denotes the reference area.

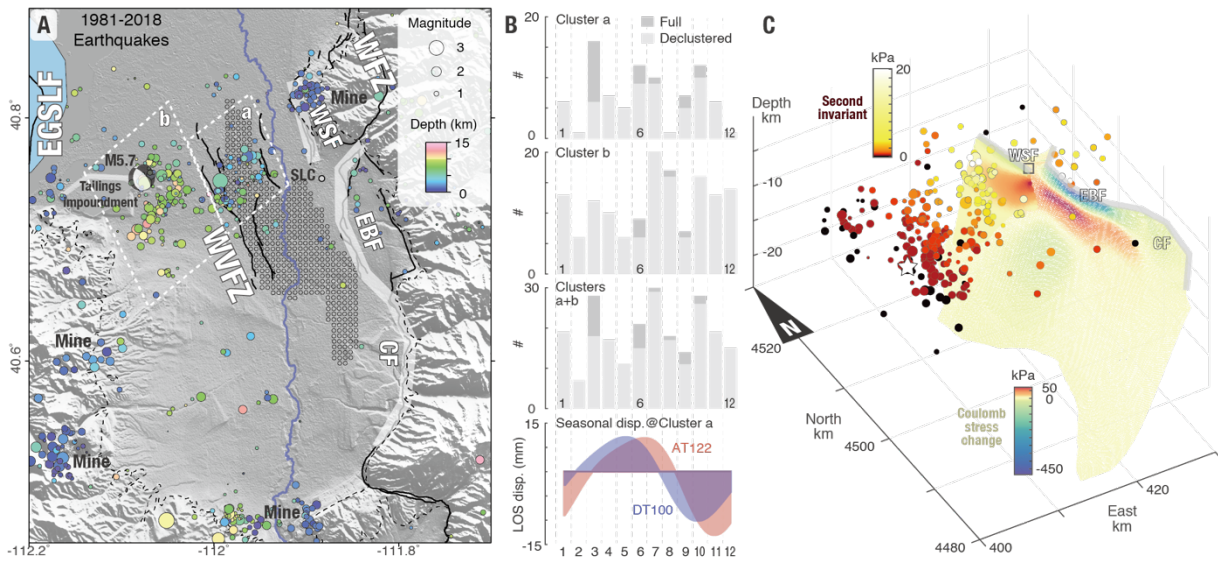




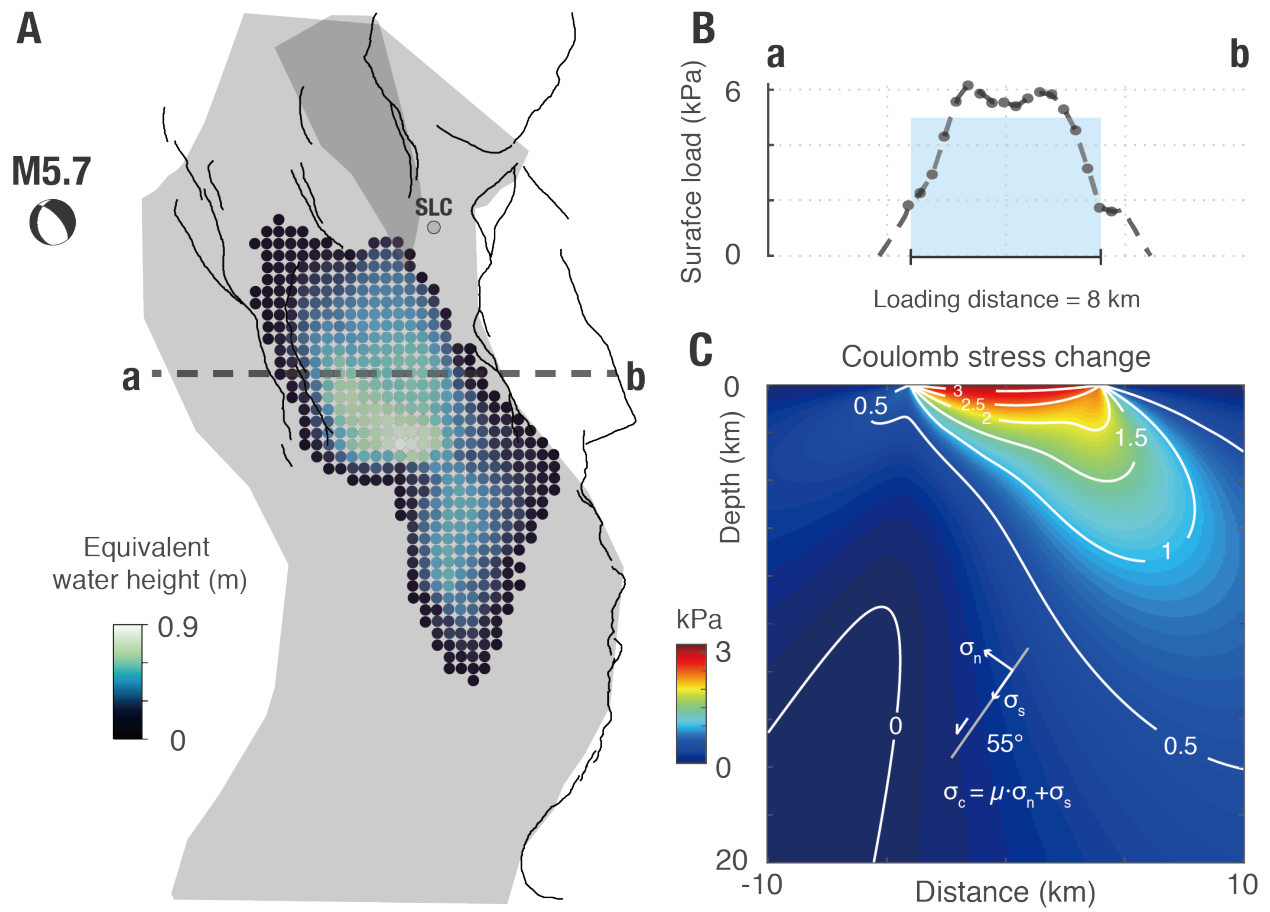
477

478 Figure 4. Map of GPS sites and water wells. (A) The locations of 5 water level wells (out of 44)  
 479 with number labels and 12 GPS stations with letter labels. Colored shades mark the hydrological  
 480 units of discharge and recharge areas. Thick black lines show the Quaternary faults. Thin lines  
 481 show elevation contours with 100-m intervals. Dotted lines outline the basin-fill deposits. (B)

482 Monthly binned water levels surrounding the EBF and WVFZ (positive values mean effective head  
483 levels above the land surface and negative values mean below the land surface). (C) 3D  
484 displacements at GPS stations ZLC1, SLCU, and UTCR overlapping in time during 2010-2014,  
485 contained in different hydrological units, and separated by the WVFZ. Complete water level and  
486 GPS plots can be found in figs. S2-S3.



487  
 488 Figure 5. Seismicity in the SLV area. (A) The distribution of earthquakes during 1981-2018.  
 489 Event locations are shown by circles whose size indicates the magnitude and the color represents  
 490 the depth. Four mining sites near the mountain fronts have shallow earthquake clusters ( $< \sim 2$  km)  
 491 and are excluded from the analysis. White thick lines show the surface traces of the principal  
 492 fault segments of the Wasatch Fault Zone around Salt Lake City, including the Warm Springs  
 493 fault (WSF), East Bench fault (EBF), and Cottonwood fault (CF). Smaller areas on either side of  
 494 the West Valley Fault Zone (WVZF) outlined by white dashed boxes (*a* and *b*) are selected for  
 495 statistical analysis. (B) Month-of-year histograms of the full and declustered earthquake  
 496 catalogue in boxes *a* and *b* and their combined areas. The bottom plot shows the seasonal LOS  
 497 displacements at the center of box *a* (red and blue shades represent AT122 and DT100 results,  
 498 respectively). In contrast, the displacements in box *b* exhibit no seasonality (fig. S12). The  
 499 March 18<sup>th</sup>, 2020 M5.7 earthquake (focal mechanism in A and hypocenter shown as a white star  
 500 in C). (C) The Coulomb stress change on the WFZ fault planes and the second invariant of stress  
 501 at each hypocenter (1981-2018) due to volume strain during peak water levels in the spring.



502

503 Figure 6. Change in Coulomb stress due to seasonal groundwater loading. (A) The layout of the  
 504 target aquifer and nearby faults in map view. (B) Surface stress from distributed line load. (C)  
 505 Springtime Coulomb stress due to seasonal groundwater changes on a profile section across the  
 506 aquifer (dashed line in A).